Modeling of Movable Control Surfaces and Atmospheric Effects

Lars Reimer and Ralf Heinrich

German Aerospace Center (DLR), Institute for Aerodynamics and Flow Technology, $C^2A^2S^2E$ Department, Lilienthalplatz 7, 38108 Braunschweig, Germany
{Lars.Reimer,Ralf.Heinrich}@dlr.de

Abstract. The paper reports on meshing strategies for modeling of movable control surfaces. In the course of the project ComFliTe, different meshing strategies have been investigated. As central test cases a generic wing-aileron configuration based on the LANN wing [1] was studied. Approaches based on mesh deformation, the Chimera technique and a combination of Chimera technique and mesh deformation were considered. As second test case a generic wing-spoiler configurations was studied. The challenging thing about the latter test case was that the simulation was supposed to start when the spoiler is still fully recessed in the contour of the wing. The pros and cons of the different modeling approaches applied to the aileron and the spoiler test case are discussed and recommendations for modeling of particularly moving control surfaces are given. In addition, the so-called disturbance velocity approach is presented in the second part of this paper as a very efficient technique for the modeling of atmospheric effects striking an aircraft; e.g. gusts.

1 Introduction

The main objective of the national research project ComFliTe was to further develop the flow solver TAU [2] and the simulation tools built around it towards capabilities for virtual analysis of flight tests and ultimately for virtual aircraft certification. In ComFliTe, among other things, the handling of moving control surfaces and the modeling of atmospheric effects such as gusts were identified as key technologies to be developed resp. enhanced.

Even though the consideration of control surfaces with fixed deflection angles has become common practice in high-fidelity CFD simulations over the last couple of years due to the improvements in unstructured mesh generation capabilities, it is still challenging to include movable control surfaces into the analysis. However, the consideration of movable control surface is an important prerequisite to enable the simulation of maneuvering aircraft and quantification of related loads. Against this backdrop, Sect. 2 of the paper at hand reports about the meshing strategies investigated in the course of the ComFliTe project for the modeling of movable control surfaces.

In industry, in order to estimate additional loads arising e.g. during gust encounters of aircraft, in many cases steady approaches are still in use. For

N. Kroll et al. (eds.), *Computational Flight Testing*, Notes on Numerical Fluid Mechanics and Multidisciplinary Design 123,
DOI: 10.1007/978-3-642-38877-4_13,

example, the additional speed of a vertical gust induces an increased angle of attack which then is used to compute an increased lift, the resulting load factor or the increased root wing bending moment needed for the sizing of the structure. In many cases, also simplified aerodynamic methods are used, like potential or strip theory, without taking into account nonlinear and unsteady behavior of the flow properly. This can lead to overestimation of the loads. To enable more realistic prediction of the loads, a gust modeling approach based on the disturbance velocity method was implemented into the TAU code during ComFliTe. Sect. 3 reports about the fundamentals of the disturbance velocity approach.

2 Techniques for Modeling of Movable Control Surfaces

In ComFliTe three approaches for enabling control surface motions in CFD simulations have been studied by DLR. They are based either purely on mesh deformation, which can be regarded as the simplest approach, or on the Chimera technique, or on a combination of the both. This section describes the investigated approaches and points out the pros and cons that have been identified during the application of the approaches to the test configuration shown in Fig. 1. The configuration represents the LANN wing configuration [1] to which a generic aileron was added. The application of each of the aforementioned modeling techniques to the geometry of the test configuration finally led to the configurations and CFD meshes shown in Fig. 2. Each of the configurations entails slight differences with respect to the configuration shown in Fig. 1 due to the applied modeling technique, i.e. whether or not and where gaps exist between aileron and wing.

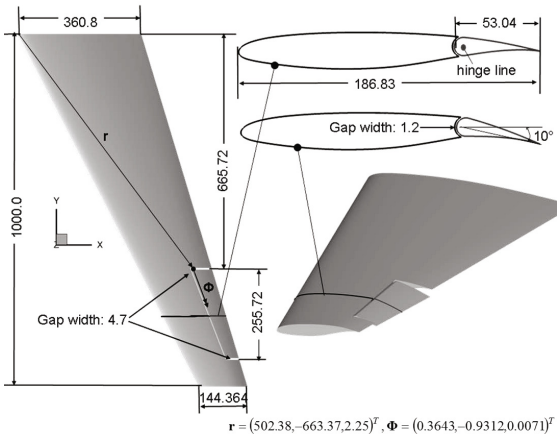

Fig. 1. Test configuration used for the investigation of different control surface modeling variants. The LANN wing configuration [1] forms the basis of the test configuration to which a generic aileron was added.

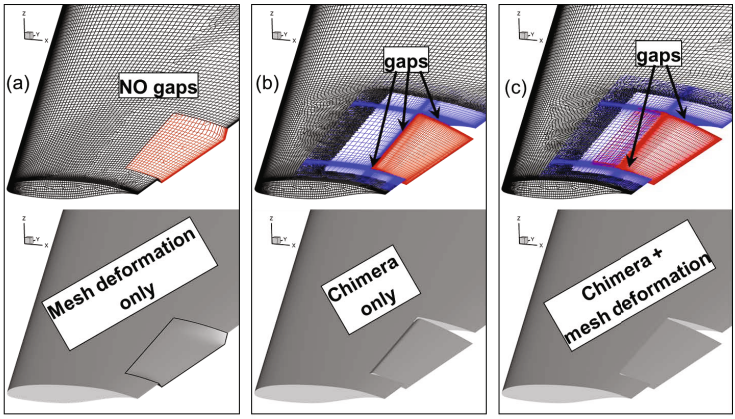

Fig. 2. Test configurations and CFD meshes used to demonstrate the differences between the investigated control surface modeling approaches: (a) aileron deflected by mesh deformation only; (b) aileron inserted and deflected by using the Chimera technique only; (c) aileron inserted by using the Chimera technique and deflected via mesh deformation; exemplarily, the aileron is deflected downwards by 10° in each sub-figure

The subsequent Sects. 2.1, 2.2, and 2.3 describe in detail how the meshes of the three chosen aileron modeling approaches are built. Qualitatively Sect. 2.4 illustrates the effects of each aileron modeling approach on the computed flow solution. Section 2.5 shows how a deploying spoiler test case can be computed with the purely Chimera-based approach.

2.1 Deflection via Mesh Deformation

This section describes the application of the mesh deformation technique for modeling moving control surfaces. The report at hand focusses on mesh deformation based on radial basis functions (RBF). However, in principal, all findings of the report at hand also apply to other mesh deformation concepts. Put simply, the concept of the RBF-based mesh deformation consists of two steps: In step 1 a polynomial approximation of the surface displacement field — often referred to as "spline" — is computed. In step 2, the computed spline is evaluated for all volume mesh points yielding the displacements for every volume mesh point. For complex configurations it is reasonable to build not only a single spline for the whole surface of the configuration, but to build each per surface component, e.g. one for the wing and one for the aileron. The displacement contributions of every spline at one volume mesh point are superimposed to a total displacement by distance-based weighting. To preserve the surface orthogonality of the grid lines, the full displacement contribution of the component spline is taken in the boundary-layer resolving mesh (weight=1). With increasing distance to the boundary-layer mesh the displacement contribution is faded out (weight $\rightarrow$ 0). For more details about the fundamentals of RBF-based mesh deformation, the

authors refer to [4,5,6]. In the work at hand the RBF-based mesh deformation method implemented in the FSDeformation code [7] was used. It is part of the FlowSimulator software environment which is being progressively developed by EADS, ONERA, DLR and universities. As is common practice, a linear global polynomial enabling rigid-body rotations of mesh components is used in FS-Deformation as basis of the displacement field approximation function. In the applications shown in the report at hand, so-called volume splines were used as RBF. The volume spline is simply the distance function between two mesh points.

The RBF-based mesh deformation approach was applied to deflect the generic aileron of the test configuration as shown in Fig. 3. Lateral gaps existing in reality between wing and aileron cannot be modeled or at least it cannot be recommended to model them when the aileron is to be deflected by mesh deformation. Otherwise, already at low deflection angles, mesh deformation would highly shear the grid cells in the gap region. The ensuing flow simulation is very likely to fail then because of poor cell qualities or even negative cell volumes. Thus, it is preferred to omit the gaps and blend the aileron deflection from full to zero deflection in the region of the gaps via mesh deformation; cf. very right Fig. 3 showing a detail view of the trailing edge of the aileron while it is deflected by 20°. Because the volume mesh generated around the LANN wing is rather coarse, cells with negative volumes appear in the vicinity of the trailing edge kinks in this case not until the aileron deflection angle exceeds 20°. In case of finer meshes degenerated cells can appear already at even much lower deflection angles. In comparison to the non-deflected aileron, Fig. 3 gives an overview about how the surface mesh and a cut through the corresponding volume mesh looks like for several aileron deflection angles, i.e. for 5°, 10°, 15°, and 20°.

For deflecting the aileron according to the desired deflection angle, two volume splines[1] were generated. One volume spline, henceforth called aileron spline, was associated to the surface segment covering the aileron; the other volume spline, henceforth called wing spline, was associated to the remaining wing surface. To fix the points on the wing surface, the displacement field of the wing spline consisted of "zero" displacement vectors at four non-planar base points. The aileron spline comprised the following displacement field: The displacement vectors of the aileron's trailing edge points, see the vector arrows in Fig. 3 (left), were computed by using the distance of the points to the hinge line (see Fig. 1) and the desired aileron deflection angle in Rodrigues' non-linear rotation formula. The points along the seam between the aileron's surface segment and the remaining wing surface also got "zero" displacement vectors to obtain the blending effect between the wing and deflected aileron.

[1] In this case the term "volume spline" denotes not only the type of RBF but the whole approximation function consisting of the linear polynomial and summation of RBF.

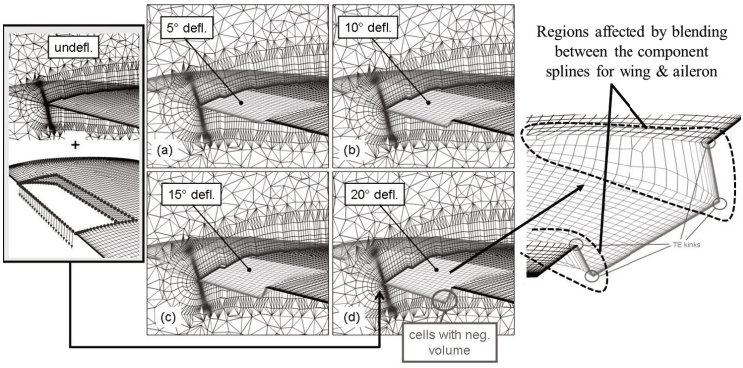

Fig. 3. Mesh deformation approach: Wing surface and surrounding volume mesh of the LANN wing with aileron resulting from a downward deflection of the aileron by (a) 5°, (b) 10°, (c) 15°, and (d) 20° by using mesh deformation only; very left sub-figure shows the mesh of the non-deflected aileron and the scattered displacement field that caused 20° aileron deflection; non-zero displacements were only prescribed at the points featuring the displacement vectors; for all other points, which are the "seam" points and those on the wing surface, zero displacements were prescribed

2.2 Deflection via Chimera Technique

The Chimera technique is the method of choice whenever large relative motions of configuration components are present — like in simulations of store separation or those that include moving control surfaces. In the work presented here the Chimera technique as is implemented in the TAU code [3] is used. With the Chimera technique, which is also known as overset grid method, several overlapping component grids are assembled to one grid. Figure 4 shall help to explain the main ideas of the Chimera concept. The figure shows a Chimera grid for the NACA0012 airfoil with movable flap. The assembled Chimera grid consists of three component grids: one farfield grid with pre-generated hole around the airfoil, one nearfield mesh around the airfoil, and one mesh around the flap. At so-called Chimera boundaries of component grids the unknown flow field values are interpolated from the other component grids that overlap the respective Chimera boundary. Chimera boundaries are either the outer boundary of a component grid (cf. the boundary marked by "outer Chimera bdry of block 2" in left Fig. 4) or they are cut as inner boundary of a component grid by so-called hole-cutting geometries (cf. the boundary the "inner Chimera bdry of block 3" in right Fig. 4).

For interpolation of the Chimera boundary points, commonly called fringe points, the overlapping component grids are searched for valid donor cells. Once a donor cell is found, the values at the fringe point are interpolated from the corner nodes of the donor cell by applying iso-parametric mapping, i.e. classical finite-element interpolation. A crucial aspect of the Chimera technique is the actual search for the donor cells. Please consider, for instance, the inner Chimera

boundaries of block 2 and 3 shown in the very right Fig. 4. Both Chimera boundaries were cut by the hole-cutting geometries shown in the middle Fig. 4. For the fringe points along the inner Chimera boundary of block 3 donor cells in block 2 are wanted. Accordingly, donor cells are wanted in block 3 for the fringe points along the inner Chimera boundary of block 2.

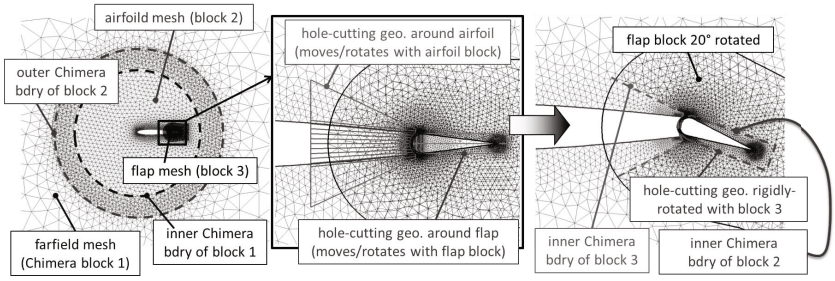

Fig. 4. Basic principle of the Chimera technique; NACA0012 sample configuration with movable flap; overall Chimera mesh is assembled from three Chimera block meshes: (1) farfield mesh, (2) nearfield mesh around NACA0012 airfoil without flap, (3) nearfield mesh around flap; very right sub-figure shows the deflected state of the aifoil's flap

Valid donor cells can only be found if sufficient overlap exists between the component grids. If there is insufficient overlap, the second-order Chimera interpolation, which is required for second-order flow solvers, cannot be accomplished. The only possible solution to fall back on is to apply nearest-neighbor interpolation, i.e. degrade the interpolation to zero order which also locally degrades the flow solution; or, as a last resort, the simulation must be stopped because of so-called "orphan" fringe points.

Though it is often presented that way, it is not true that the component grids in a Chimera grid can be generated completely independently of each other. During generation of the component grids it must already be considered that there has to be sufficient overlap between the component grids. Especially, if component grids move relative to each other, the change of the Chimera boundaries, in particular those created by hole-cutting, must be anticipated and taken into account carefully during grid generation. In consequence, the region in the donor mesh through which the recipient mesh is moving should feature almost uniform cell sizes.

Very special diligence must be exercised in the generation of the component grids that overlap in small gaps; cf. detail views in Fig. 5. In general, such gaps must exist in order to be able to rotate Chimera blocks containing control surfaces, i.e. in order to be able to actually deflect control surfaces by using solely the Chimera technique. The major disadvantage when applying solely the Chimera technique for control surface modeling is that, though the user is not interested in the flow solution in the gap across the main flow direction, many grid cells have to be spent in the gap only for the sake of providing sufficient Chimera interpolation overlap.

Besides the factors influencing the component mesh generation process that have already been mentioned, the following further considerations have to be taken into account:

- For the sake of interpolation quality, similar cell sizes in the overlap region of recipient and donor grid are recommended.
- To get rather clear-cut Chimera boundaries along hole-cutting geometries instead of rather frayed ones which promote the existence of orphan points, small cell sizes are preferred in regions that are affected by hole-cutting.

In principle, the Chimera technique brings much flexibility to the mesh generation process and enables the simulation of problems with relative motion in the first place. However, the preparation process of a Chimera grid can be a very cumbersome task if no tool is available that automatically takes care of all aforementioned dependencies between component grids. Without such a tool the user has to generate and modify in a trial-and-error process the component grids and the corresponding hole-cutting geometries until no orphan fringe points exist in the assembled Chimera grid.

In the following the concept of the purely Chimera-based aileron modeling approach is explained, which in the application to the LANN wing test configuration turned out — after several attempts — to be the only feasible approach at all. Figure 5 presents the assembly of the Chimera grid from a background grid and two component grids. An unstructured mesh suitable for RANS simulations of the clean-wing LANN configuration serves as Chimera background grid. It was generated using ARA's SOLAR[2] mesher. The right Fig. 5 shows how the part that is to be replaced by a movable aileron is cut out of the background grid. The cyan-colored box in the figure represents the applied hole-cutting geometry. The first component mesh inserted into the free space created in the background grid is shown in the middle Fig. 5. It contains a structured mesh for the aileron cutout geometry. The second component mesh shown in the left Fig. 5 represents the volume mesh around the aileron. It is a structured mesh, too.

Structured Component Grids. Structured meshing was chosen for both component grids since it is by far easier to setup proper Chimera overlap between structured meshes than between unstructured meshes; especially if the meshes are subjected to relative motion. This holds because unstructured grid generators tend to chop off the outer layers of the near-body grid or pull it back close to the surface in areas of significant geometry changes. In the farfield grid, which is attached to the near-body grid, the size of the tetrahedrons grows rapidly with increasing distance to the surface. In particular, in situations when near-body grid chopping is very likely to happen, e.g. in very narrow gaps such as between aileron and aileron-cutout, it is often very difficult and sometimes appears to

[2] SOLAR is an unstructured mesh generator developed by ARA (England's Aerospace Research Association) which creates hexahedron-dominant nearfield meshes on which tetrahedron-dominant farfield-filling meshes are constructed.

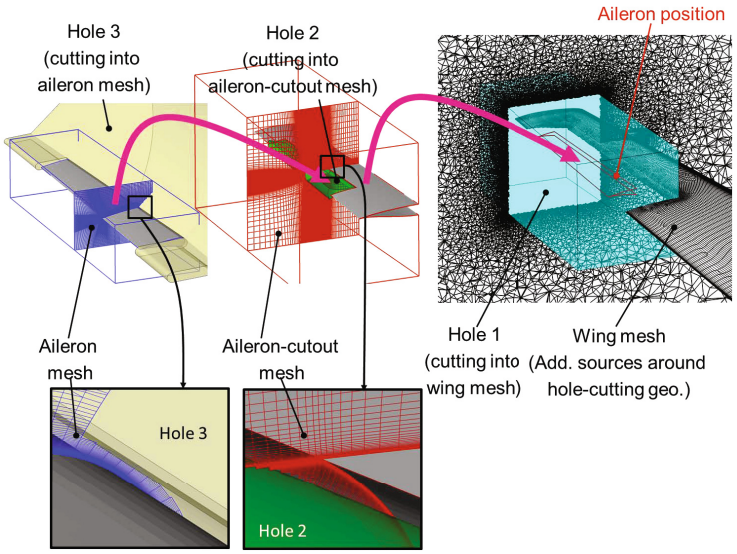

Fig. 5. Purely Chimera-based modeling approach: concept for the assembly of the Chimera grid of the wing-aileron configuration in which the aileron is deflected by applying the Chimera technique only; the Chimera block containing the aileron is subjected to rigid-body rotations around the aileron's hinge line defined in Fig. 1

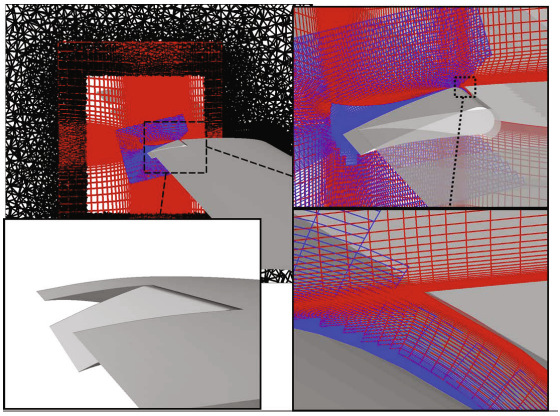

Fig. 6. Purely Chimera-based modeling approach: insight into the assembled Chimera volume grid for a deflected aileron state; black mesh = unstructured background mesh around LANN wing; red mesh = inserted structured component mesh generating the aileron cutout; blue mesh = inserted structured component mesh around aileron

be even impossible to control the cell size in unstructured component grids in such a way that the required overlap between the overlapping Chimera grids is obtained. In contrast to unstructured grids, the cell size in the overlap region can be precisely controlled during mesh generation by the user in structured component grids. The structured grids shown in the report at hand were generated by using ANSYS' ICEM-CFD Hexa mesher.

Modification of the Background Grid Towards the Inserted Component Grids. To generate tetrahedron fringe cells in the unstructured mesh which match the size of the fringe cells in the inserted component grids, i.e. for creating proper Chimera overlap, sources were added along the hole-cutting geometry during mesh generation of the unstructured background grid; see Fig. 13 illustrating the resulting effect for the spoiler case as well as the right Fig. 5 showing the resulting mesh refinement along the cyan-colored box for the aileron case. The final approach originated from several unsuccessful previous attempts in which was claimed not to modify at all the unstructured background grid. The restriction originated from the desire to add control surfaces without much effort to existing well-converging unstructured grids. But the preparation of proper Chimera overlap between unstructured background grid and inserted structured grids caused severe difficulties. For many Chimera fringe points in the tetrahedron part of the unstructured grid, no donor cells could be found; cf. Fig. 13 illustrating the aforementioned things for the spoiler test case. In the unmodified unstructured grid the size of most tetrahedron cells in direct vicinity of the Chimera boundary is already too big compared to the width of the overlap region. Sometimes it is possible, though not welcome, to solve the issue by increasing significantly the overlap extent or by reducing extremely the size of the hole-cutting geometry. However, sometimes even those actions cannot be taken because of prevailing conditions. In consequence, the original claim was abandoned and it was tolerated to adapt the background grid towards inserted component grids.

Hole-Cutting Geometries. For the pursued concept of integrating the aileron in the configuration, three hole-cutting geometries as shown in Fig. 5 are required. The most challenging task is the preparation of the holes labeled 2 and 3. Not the actual generation is challenging, but the fine-tuning of the hole shapes so that no orphan fringe points appear. The holes must be carefully designed with respect to the properties of the component mesh which they are cutting into. In the gap across the main flow direction extending along the hinge line both holes must be very close to the solid wall so that sufficient overlap remains between both component grids in the gap. This also applies to the shape of the hole geometries in regard to both gaps existing in spanwise direction. In addition, hole 3 must even extend in spanwise direction over the wing surface because of the trapezoidal planform of the aileron. Due to the planform the aileron mesh can intersect with the wing while the aileron gets deflected. Therefore, hole 3 is supposed to blank all cells of the aileron mesh before intersecting with the wing.

In combination with the design of hole 3, it must be taken also into consideration during the generation of the aileron mesh that it does not get too coarse at its outer boundary. Otherwise, the Chimera boundary in the aileron mesh cut by hole 3 might come too close to the Chimera boundary in the aileron-cutout mesh cut by hole 2 which would result in "orphan" points.

The wedge-like shape of hole 3, see Fig. 5 , extends towards the wing's leading edge as to prevent the aileron mesh from intersecting with the Chimera boundary between aileron-cutout mesh and background mesh. Otherwise, orphan fringe points would appear in vicinity of the intersection once the aileron mesh gets too close to the respective boundary which in turn whould also entail the appearance of "orphan" points.

The surface mesh of the configuration with aileron, which results from assembling background grid and component grids in the way explained before, is shown in the middle of Fig. 2. Exemplarily, Fig. 6 shows details of the assembled Chimera volume grid while the aileron is deflected downwards.

A certain advantage of the presented approach is that, once the user has completed the assembly process of the Chimera grid being all too often very cumbersome, upward and downward aileron deflections, even very extreme ones, can be simulated without further effort. As part of the flow computation the component mesh around the aileron just is to be rigidly rotated around the aileron's hinge line by the aileron deflection angle.

One downside of the approach is certainly the large number of grid points; cf. Table 1. Very many grid points are required just for the sake of providing sufficient Chimera overlap, in particular in the gap along the hinge line. From the flow physics point of view another disadvantage of the gap is that it is also just required for enabling the rotation of the aileron mesh, though coverings of the gaps prevent flow-through at real aircraft.

2.3 Deflection via a Combination of Mesh Deformation and Chimera Technique

Some of the drawbacks of the purely Chimera-based control surface modeling approach can be avoided when mesh deformation and Chimera technique are combined. The motion of Chimera blocks, such as the rotation of the aileron mesh in Fig. 6, increases the complexity during the preparation of the Chimera case considerably. If not large relative motion between Chimera blocks is to be simulated, it is thus more practical to fix the respective Chimera blocks in space and obtain moderate control surface motions by mesh deformation. The Chimera technique is applied in this approach to consider the spanwise gaps between aileron and wing in the analysis. Since the gaps affect the aircraft's wake pattern and accordingly also its overall circulation, they ought to be considered. In contrast to the approach that is based purely on mesh deformation, with the combined Chimera/mesh deformation approach we do not need to be afraid of excessive shearing of cells in the gap region — thanks to the combination with the Chimera technique. Because mesh deformation is used to actually deflect the aileron, the gap can now be omitted that runs across the main flow direction and

in which many points had to be put resp. "wasted" in the purely Chimera-based approach just for providing sufficient Chimera overlap.

In the following the combined Chimera/mesh deformation is presented for the LANN wing test case with movable generic aileron. Figure 7 illustrates the assembly instructions of the Chimera grid. At first glance, the concept looks very similar to the purely Chimera-based one. However, decisive differences exist.

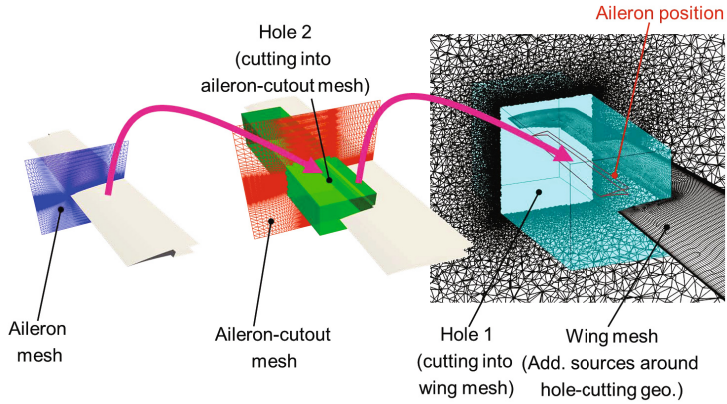

Fig. 7. Combined Chimera/mesh deformation approach: concept for the assembly of the Chimera grid of the wing-aileron configuration in which the aileron is deflected by mesh deformation; the Chimera blocks in the overall Chimera grid are not subjected to relative motions — they are fixed in space

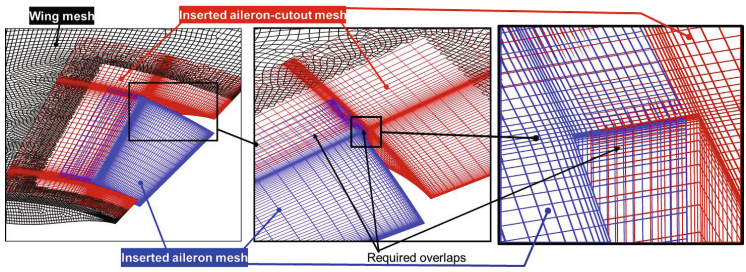

Fig. 8. Combined Chimera/mesh deformation approach: Chimera overlap between both inserted structured component meshes

Hole-Cutting Geometries. The hole-cutting geometries are different than in the purely Chimera-based approach. Not only that no longer three but only two hole-cutting geometries are required. Their shapes are also much simpler. Just like the inserted component grids, both holes are simply cuboid-shaped. Thus, the holes can be generated much easier than the ones with the much more complex shapes needed in the purely Chimera-based approach.

Structured Component Grids. Due to the same reasons as in the purely Chimera-based approach, the usage of structured component grids is favored over unstructured ones. With the combined approach, however, the mesh generation process of the component grids is a bit easier, because no additional overlap scenarios resulting from Chimera block motions have to be anticipated. There is just one unchanging Chimera overlap representing the undeflected aileron state to be prepared during mesh generation. A detail view on the Chimera overlap between the component grids in the gap region is presented in Fig. 8.

Modification of the Background Grid Towards the Inserted Component Grids. Since the same hole-cutting geometry is used, i.e. the cyan-colored box in Figs. 5 and 7, the very same modified background grid as in the purely Chimera-based approach is applied in the combined Chimera/mesh deformation approach.

Control Surface Deflection via Mesh Deformation in the Inner Chimera Block. The aileron is deflected by applying mesh deformation in the same manner as with the purely mesh deformation-based approach. However, with the combined approach not the whole mesh is subjected to mesh deformation but only the Chimera block that contains the aileron.

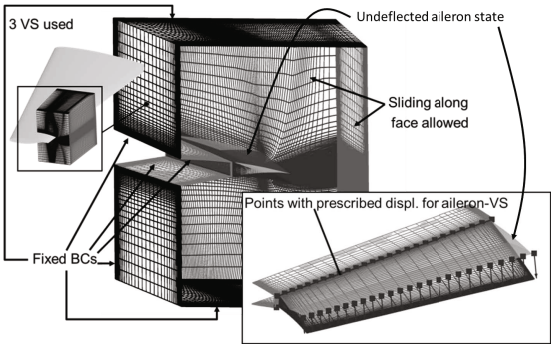

Fig. 9. Combined Chimera/mesh deformation approach: boundary conditions used during mesh deformation applied to the aileron Chimera block only for deflecting the aileron (VS denotes "volume spline")

The mesh deformation boundary conditions imposed to the outer boundaries of the respective Chimera block are presented in Fig. 9. While the grid points on top and bottom boundary of the aileron Chimera block, as well as the ones on the upper and lower inflow boundaries, may be fixed, it is important that the grid points on both lateral boundaries and on the outflow boundary can slide along the respective boundary planes. Otherwise, no benefit is to be expected from the Chimera technique because the grid cells located in the spanwise gaps

would still be sheared and cells with negative volume would most likely occur. Exemplarily for 20° downward aileron deflection, Fig. 9 shows the mesh on the boundary of the Chimera block after applying mesh deformation only to that block.

The hole-cutting geometry 2 in Fig. 7 should also be deformed in the same way as the aileron; i.e. the same scattered displacement field that causes the wanted aileron deflection should be applied to deform the hole mesh. Otherwise, the deflected aileron might leave the volume cut out by the undeformed hole so that "orphan" points would occur very likely.

Table 1. Comparison of the number of grid points each of the three discussed aileron modeling approaches entails; grid point numbers are in millions; meshes marked by asterisk include 2.3 million points in the background grid instead of 1.6 million

Mesh deformation	Chimera	Mesh defo./Chimera
1.6	15.3*	6.2*

2.4 Flow Simulation of the Deflected Generic Aileron Case

In Fig. 8 the flow solution for 10° downward aileron deflection resulting from applying the purely mesh deformation-based approach is compared to the ones obtained with the purely Chimera-based approach and the combined Chimera/mesh deformation approach. Because of the differences in the discretization of the wing surface in the regions where background grid and component grid overlap, it was mandatory to apply the Chimera wall projection [8]. In the computations the tolerated mismatch between overlapping walls was set to 0.001. The flow conditions at the farfield boundary was set to zero angle of attack, Mach number 0.82, and Reynolds number 7.2 million. (Reynolds length is 0.3608.)

The flow solutions are compared in terms of pressure distributions on wing and aileron surface, as well as in terms of the distribution of the eddy viscosity in the wake of the wing. It must be admitted though that the unmodified background grid is a rather coarse grid. The modified wing grid that is used in the approaches involving the Chimera technique is slightly refined around the inserted aileron. Moreover, the inserted structured Chimera blocks are significantly finer than the unstructured background grid. This can be noticed in particular in the flow solution which appears to be quite "smeared out" in the nearfield wake of the aileron. The differences in the surface pressure distribution are primarily caused by modified wake structures. In contrast to the modeling approach which relies on mesh deformation only, the approaches involving the Chimera technique clearly resolve the vortices generated by both spanwise gaps. And, since the inserted component meshes feature much finer grid resolution and thus are less dissipative than the background grid, the vortical flow structures caused by the gaps and incipient separation on the aileron surface also survive farther downstream in the structured component meshes. But as soon as the wake leaves

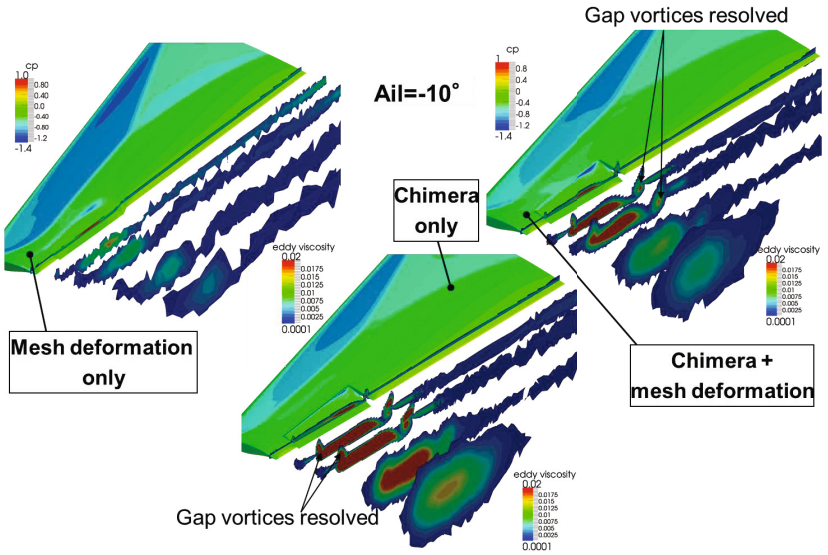

Fig. 10. Comparison of the flow solutions of the three pursued aileron modeling approaches in terms of surface pressure distribution and eddy viscosity in four planes cut through the wing wake parallel to the wing's trailing edge (lower threshold for eddy viscosity is 0.0001); the aileron is deflected downwards by 10° in all cases

the component meshes and enters the coarse tetrahedron background mesh, the wake vortices dissipate, as can be observed in the flow solutions shown in the middle and right Fig. 10. Further observations from Fig. 10 are that the gap vortices and the shear layer downstream of the aileron are the most pronounced with the purely Chimera-based approach.

For a final assessment of the different modeling approaches with respect to the the capturing of flow features, it is planned — since it has been beyond the scope of the ComFliTe project — to conduct an additional thorough grid convergence study and to compare also the influences of the modeling approaches at other angles of attack and aileron deflection angles. Nevertheless, recommendations have been derived from the investigations made so far and are given in Sect. 2.6 of the report at hand.

2.5 Flow Simulation of the Deploying Generic Spoiler Case

A spoiler configuration was simulated with the purely Chimera-based approach. It was not reasonable to use the mesh deformation approach or the approach which combines mesh deformation and Chimera technique, because, in the sense of a feasibility study, it was planned to simulate large spoiler motion starting with the situation in which the spoiler is fully recessed in the contour of the wing. During the simulation the spoiler should be deployed up to 40 degrees in

increments of 5 degrees. For every increment a steady flow simulation was supposed to be performed based on a restart from the flow solution of the previous increment. The drawing in Fig. 11 shows the dimensions of the resulting configuration with non-deployed spoiler including information about the gap dimensions as well as the location and orientation of the hinge line. The basis of the moving spoiler configuration chosen here is also the LANN wing. Exemplarily, in the right of Fig. 11, a view on the configuration with 30°-deployed spoiler is presented.

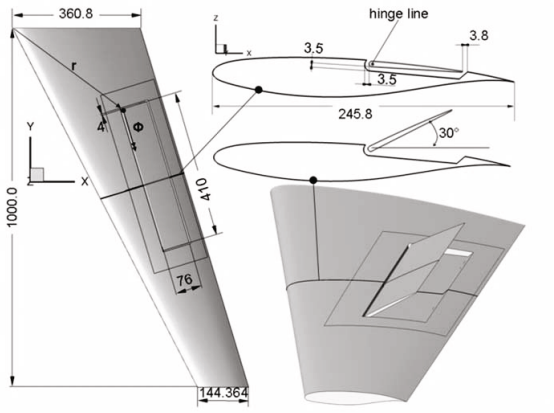

Fig. 11. Spoiler configuration: Overview of the geometry; the wing corresponds to the LANN wing [1]; dimension are in millimeters

Fig. 12 presents the meshing concept pursued for the moving spoiler configuration. It is almost identical to the one of the purely Chimera-based approach of the LANN wing with aileron shown in Fig. 5. In order to add the spoiler to the clean-wing configuration two structured component meshes were generated: one representing the spoiler cut-out geometry and the other one discretizing the flow volume around the moving spoiler.

Fig. 13 illustrates the modifications made in the unstructured background mesh of the spoiler configuration which were already discussed in the sections of this report which describe the pursued aileron modeling approaches. Without the modifications shown in the right Fig. 13 many "orphan" points exist. With modifications, i.e. by arranging additional sources in the SOLAR meshing process along the boundary of hole H1, the fringe points in the background mesh follow very closely the shape of the hole so that all "orphan" points disappear. The resulting modified Chimera grid of the spoiler configuration which includes the modified background grid has 8 million grid points. The flow conditions used in the moving spoiler case were chosen identical to the ones used for the aileron cases.

The whole solution process with TAU for the deploying spoiler case was as follows: For the undeployed spoiler, at first a three-stage solution sequence was

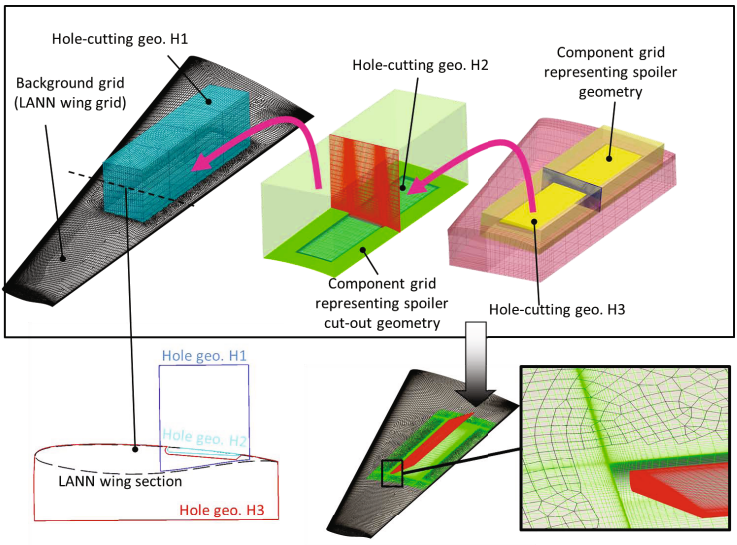

Fig. 12. Spoiler configuration: overview of the concept for the assembly of the Chimera

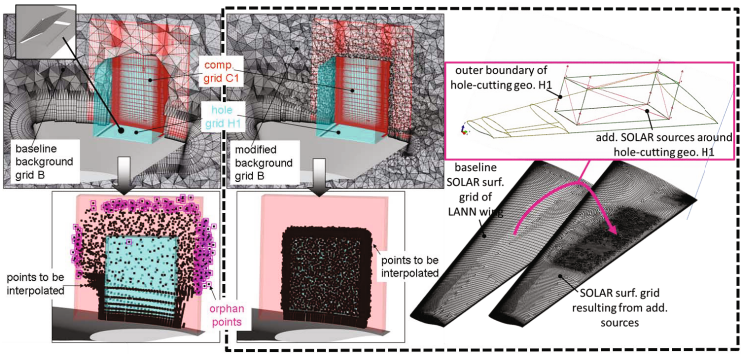

Fig. 13. Spoiler configuration: effect of the additional SOLAR mesh generation sources arranged around hole H1 on the background grid and in consequence on the distribution of Chimera interpolation points; left: unmodified background grid with many "orphan" fringe points; right: modified background grid without "orphan" points

executed: The first stage comprised 20000 three-level V-type multi-grid iterations including 5000 start-up single-grid iterations. Inviscid fluxes were discretized by a first-order van Leer upwind scheme. At the second stage it was switched to the second-order scheme for additional 20000 iterations. At the third stage Jameson central scheme with scalar dissipation was used. Although it is not designed to be used for massively separated flow, just to simplify matters, the Spalart-Allmaras turbulence model was applied. Multi-grid acceleration was not applied to the turbulence equations. The convective fluxes in the turbulence equations were solved by first-order Roe scheme. For steady-state time integration a three-stage Runge-Kutta method with constant CFL numer of 0.8 was applied. After a converged solution has been computed for the undeployed spoiler, a sequence of steady simulations was conducted. After each increment of 5 degrees TAU was restarted from the previous flow field solution beginning each time again with 5000 single-grid start-up iterations. Afterwards between 80000 and 10000 three-level multi-grid iterations were executed. The whole simulation of the deploying spoiler was performed on 144 cores and lasted in total about 16 days.

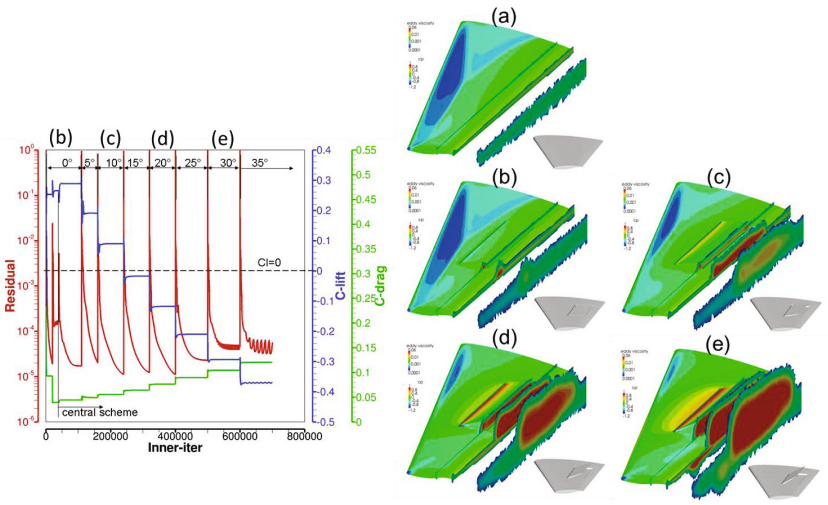

Fig. 14. Spoiler configuration: Left: convergence history of the flow solver (note the aerodynamic coefficients have not been adjusted for the Chimera overlap existing on the surface of the configuration; see Fig. 12); Right: Flow solutions for the wing configuration without spoiler (a) compared to selected solutions of the configurations with spoiler: (b) 0°, (c) 10°, (d) 20°, (e) 30° deployed spoiler; pressure distribution on the surface is shown and the distribution of the eddy viscosity is plotted in three cut-planes through the wake of the configuration oriented parallel to the wing's trailing edge

The left Fig. 14 shows the convergence history of the flow solver in terms of density residual, lift and drag coefficient for the whole simulation run. (Lift and drag coefficients are not corrected for the existing Chimera surface overlap.)

The simulation was stopped when the spoiler was deployed at 35°. At that point the oscillations in the convergence history of the lift coefficient indicate that the flow field is no longer stationary so that further stationary simulations are meaningless.

The flow solutions for selected spoiler settings are presented qualitatively in the right Fig. 14. The figure shows the surface pressure distribution and the distribution of the eddy viscosity (clipped at 0.0001) in three cut-planes through the wake of the spoiler configuration. For the sake of completeness, the solution for the clean LANN wing configuration without spoiler was added. The authors did not attach great importance in the physical accuracy of the simulations rather than on the feasibility. The report at hand demonstrates for the chosen spoiler configuration, which is admittedly yet very generic and simple, that the simulation of a deploying spoiler can be peformed — though it is computationally expensive and challenging.

2.6 Conclusions

This section shall summarize the major findings about the investigated control surface modeling approaches. The approach purely based on mesh deformation, henceforth in this section addressed as "approach (1)", has the major advantage that it requires very little preparation time. Of course, the approach also requires the fewest number of grid points; cf. Table 1. For reasons of fairness it must be noted though that due to the refinement of the background mesh around the hole-cutting geometry the purely Chimera-based approach, labeled "approach (2)", and the combined Chimera/mesh deformation approach, labeled "approach (3)", both include a wing mesh that has 2.3 million points instead of 1.6 million. However, the provision of sufficient Chimera overlap causes at the best, i.e. in the case of the combined Chimera/mesh deformation approach, three times more grid points than the pure mesh deformation approach. Since the grid size remains the same for the purely mesh deformation-based approach as for the clean configuration, the computational time is identically low. Spanwise gaps though are not considered so that the influence of gap vortices that alter with the deflection angle of the control surface cannot be captured. Approach (1) can model just fairly reasonably the effects of low to moderate control surface deflections on integral aerodynamic coefficients. Because of the proneness for the occurrence of cells with negative volumes, approach (1) may only be applicable to smaller deflection angles, especially in applications with very fine meshes. Sometimes, in the case of very coarse Navier-Stokes meshes as in the case of the unstructured LANN wing grid used in the report at hand (cf. Fig. 2 left) or in the case of Euler meshes, deflection angles between 10° and 20° may be attainable though, but the accuracy of the computed flow solution is very questionable, in particular when it comes to predicted local effects in the vicinity of the deflected control surface. Despite all criticism of approach (1) it is an efficient and very practical approach though. It reveals most of the effects and trends caused by deflected control surfaces — at least in terms of integral aerodynamic coefficients. Beside the application of approach (1) for aileron motion, the authors think

that especially for the modeling of horizontal tail-plane motions required in longitudinal trim scenarios of aircraft, mesh deformation is the best choice.

In contrast to approach (1), approaches (2) and (3) resolve spanwise gaps by utilizing the Chimera technique. Thus, they resolve vortices originating from the gaps so that both approaches feature improved physical modeling of the deflected control surface. However, both approaches also come along with the cost of way more elaborate mesh preparation and significantly increased mesh point numbers; cf. Table 1. The drawback of the increased effort to be made in mesh generation with approaches (2) and (3) may be alleviated by replacing the cumbersome manual tuning of Chimera component meshes, their assembly, and the preparation of hole-cutting geometries by an automatic generation procedure. Comparing all three approaches, approach (3) turns out to be the best compromise between preparation time, computational cost and solution accuracy. With approach (2) way too many grid points have to be spent just for the sake of the Chimera overlap in the gap across the main flow direction and due to the relative motion of the Chimera block containing the control surface. Moreover, since the gap across the main flow direction is usually covered at wings of real aircraft, approach (3) renders even better the real flow physics around deflected control surfaces. In contrast to approach (1), by applying mesh deformation just to the Chimera block that contains the control surface, the influence of the mesh deformation, which always involves alterations of the volume mesh quality, is limited in approach (3) automatically to the vicinity of the control surface.

Additionally, it has to be stated that it turned out to be the best to use structured component Chimera meshes instead of unstructured ones. The overlap between structured component meshes can be controlled by far more easily than with unstructured component meshes. Sometimes Chimera component meshes can be added to existing unstructured meshes without modifying these. In most cases though, the unstructured background mesh needs to be adjusted towards the component meshes which are supposed to fill the hole that was cut into the unstructured background mesh.

Depending on the type of application each of the approaches followed through can be reasonable — even approach (2); mind the movable spoiler case. However, it is recommended to use approach (1) to get an overview about control surface deflection trends and approach (2) for a more detailed analysis.

3 Techniques for Modeling of Atmospheric Effects

3.1 Disturbance Velocity Approach

To allow the simulation of an aircraft interacting with atmospheric effects, e.g. gusts, several approaches are possible. In [9] the wake vortex encounter of a generic aircraft configuration has been simulated with DLR's block-structured FLOWer code [10] by prescribing the incoming vortices of the preceding aircraft at the inflow boundary of the computational domain. The approach, henceforth called "full" approach, allows computing the mutual interaction of the aircraft

and the wake vortices. A fairly good agreement with experimental data measured in the frame of the European project WAVENC [11] was found. However, the full approach requires very high spatial mesh resolution so that vortices are not destroyed by numerical dissipation while being transported towards the aircraft. In order to reduce the numerical effort, a so-called disturbance velocity approach was implemented in FLOWer [12]. Though it disregards the influence of the aircraft on the wake vortices, it allows capturing the effects of the vortices on the aircraft as good as with the full approach, but can be used with the standard mesh resolution which was used for regular CFD analysis in cruise flight scenarios.

Motivated by the success of the method in the WAVENC project, the disturbance velocity approach was also implemented into DLR's unstructured solver TAU to conduct the gust encounter simulations that are presented in [13] as part of the book at hand.

In disturbance velocity approach the standard finite-volume-type flux balancing of flow solvers based on the Reynolds-averaged Navier-Stokes equations like TAU is slightly altered. Upon the velocity $\boldsymbol{v}_b$, which typically represents the cell face velocity in flow solvers with Arbitrary-Lagrangian-Eulerian formulation, an additional disturbance velocity field $\boldsymbol{v}_i$ can be superimposed very easily. The convection velocity $\boldsymbol{v} - \boldsymbol{v}_b$ across the cell interface of a control volume just needs to be replaced by $\boldsymbol{v} - \boldsymbol{v}_b - \boldsymbol{v}_i$.

Figure 15 shall make the things aforementionend a little bit clearer. It shows a gust of wave length λ moving with speed $\boldsymbol{v}_{inf} = (u_{inf}, 0)^T$ relatively to an airfoil. The shape of the gust, in this case, is specified as a function of the coordinate x and time t. In the left Fig. 15 showing the situation at time t=0, the gust is still in front of the airfoil. Thus, the velocity induced by the gust at the interface of the control volume is zero. In the right Fig. 15 at t=t_1 the situation is different — the gust is right beneath the airfoil. The local effect of the gust on the airfoil in this case is approximately the same as if the airfoil is moving with negative gust vertical speed $\boldsymbol{v}_{gust}\,(x,t)$ downwards.

In order to verify the implementation of the disturbance velocity approach in TAU, a simple so-called "equivalent test case" was used. As reference, the flow around an RAE2822 airfoil was computed for a Reynolds number of 6.3 million, and the Mach number 0.73 (corresponding to the flow speed u_{inf}). The angle of attack α was set to 2.8°. The scenario is illustrated in the left top Fig. 16. The equivalent flow scenario is the following: an inflow with velocity $u_{inf} \cos\alpha$ combined with a gust of infinite wave length and amplitude $u_{inf} \sin\alpha$. The latter scenario is depicted in the left bottom Fig. 16. The right part of Fig. 16 compares both kinds of simulation by means of the resulting c_p distributions. As expected, no differences between reference and equivalent case are noticable.

In TAU gusts can be prescribed by means of analytical functions. For all implemented types amplitude and wave length are parameters that can be specified by the user. Both vertical and lateral gusts can be feed into the flow field and can be superimposed. The user can select between isolated gusts and sequences of gusts. The extension of the gusts in spanwise direction (vertical gusts) and

vertical direction (lateral gusts) can also be specified. Figure 17, for instance, shows a generic fighter aircraft that encounters "1-cos"-shape gusts — a sequence of vertical gusts and one lateral gust. Exemplarily, Fig. 18 demonstrates for a simple NACA0012 airfoil test case that the implementation of the disturbance velocity approach in TAU works as expected when a single vertical gust (red curve) resp. a sequence of three vertical gusts (blue curve) strikes the airfoil. Corresponding to the chosen gust type the amplifications of the lift force can be clearly observed in Fig. 18.

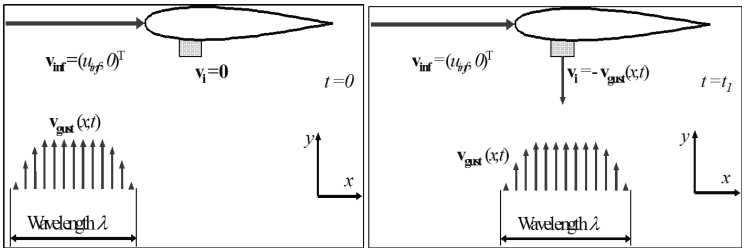

Fig. 15. Gust traveling relative to an airfoil; left: gust velocity field not yet beneath the airfoil — induced flow velocity is zero; right: gust velocity beneath the airfoil — induced flow velocity $\boldsymbol{v}_i$ is equal to gust velocity $\boldsymbol{v}_{gust}$

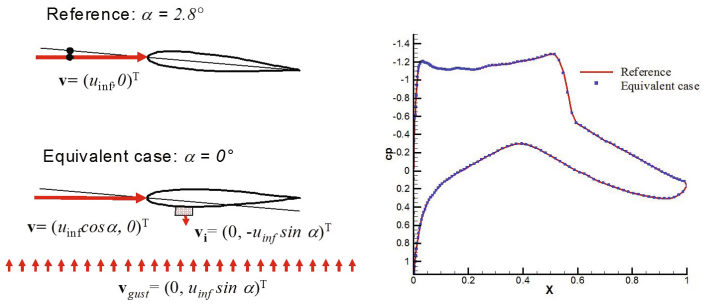

Fig. 16. Left: Reference and equivalent test case for the verification of the disturbance velocity approach. Right: Comparison between c_p distribution of reference case and equivalent test case

For further reading about applications of the disturbance velocity approach, it is referred to [13]. In the publication in the book at hand two kinds of application can be studied: (1) the simulation of the encounter of the generic fighter shown in Fig. 17 with a lateral gust; and (2) the simulation of the encounter of an A340 cruise configuration with a vertical gust taking also into account the aircraft's structural deformation during the gust encounter.

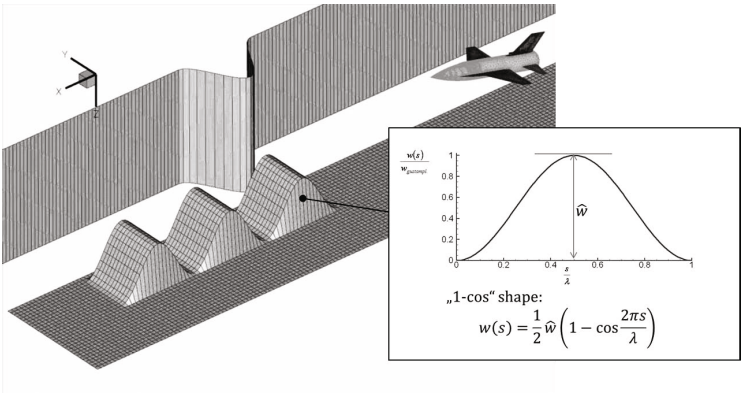

Fig. 17. A generic fighter aircraft encountering a sequence of three “1-cos”-shape lateral gusts (with limited extension in spanwise direction) and a single “1-cos”-shape vertical gust

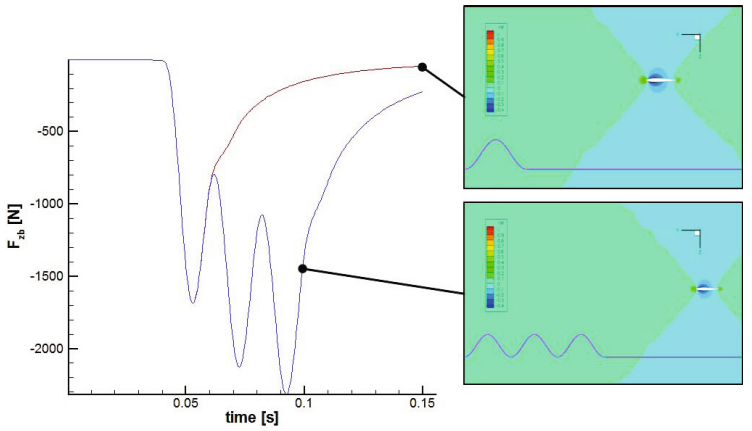

Fig. 18. Time histories of the vertical force acting on the airfoil during the interaction with a single vertical gust (red curve) and a sequence of three vertical gusts (blue curve)

4 Summary

The paper at hand reports about the developments/findings in the ComFliTe project that are of particular use for simulations of aircraft maneuvers and gust interactions with high-fidelity CFD; i.e. (1) a study of techniques for modeling of moving control surfaces, and (2) techniques for modeling of gusts. A purely mesh deformation-based control surface modeling approach, a purely Chimera-based one and a combination of the both were considered. Although the study on the control surface modeling cannot be considered yet to be complete, it can

be stated though that the pure Chimera-based modeling approach is computationally too expensive due to very high grid point numbers and also too costly in terms of preparation time — at least without having automatic Chimera grid generation tools at hand. In contrast, the combined mesh deformation/Chimera approach turns out to be the best compromise between preparation time, computational cost and solution accuracy. Additionally, the use of structured component Chimera meshes instead of unstructured ones emerged as the best option. By doing so, the Chimera overlap between structured component meshes can be controlled by far more easily.

As second topic, the principles of the disturbance velocity approach which has been implemented into the TAU code in the course of ComFliTe are explained in this paper. The approach has turned out to be an efficient tool to simulate the interaction of aircraft with gusts with CFD methods and to compute the additional loads caused by striking gusts. The efficiency of the approach arises from the fact that no additional mesh refinement or higher-order CFD analysis is needed. The very same CFD mesh and discretization order can be used as for the regular CFD analysis.

References

1. Zwann, R.J.: Data set 9, LANN wing. Pitching oscillation. Technical report. Agard-R-702 Addendum no. 1, AGARD, Amsterdam, The Netherlands (1985)
2. Schwamborn, D., Gerhold, T., Heinrich, R.: The DLR TAU-Code: Recent Applications in Research and Industry. In: Proc. of the European Conference on Computational Fluid Dynamics, ECCOMAS CFD 2006, Delft, The Netherlands (2006)
3. Madrane, A., Raichle, A., Stürmer, A.: A Parallel Implementation of a Dynamic Overset Unstructured Grid Approach. In: Proc. of the European Conference on Computational Fluid Dynamics, ECCOMAS CFD 2004, Jyväskylä, Finland (2004)
4. De Boer, A., van der Schoot, M., Bijl, H.: Mesh deformation based on radial basis function interpolation. Computers & Structures 85, 784–795 (2007)
5. Michler, A.K.: Aircraft control surface deflection using RBF-based mesh deformation. Int. J. Num. Meth. Eng. 88(10), 986–1007 (2011)
6. Rendall, T.C.S., Allen, C.B.: Efficient mesh motion using radial basis functions with data reduction algorithms. J. Comp. Phys. 228(17), 6231–6249 (2009)
7. Stickan, B.: Implementation and Extension of a Mesh Deformation Module for the Parallel FlowSimulator Software Environment. Diploma thesis, RWTH Aachen University, Chair for Computational Analyis of Technical Systems (2009)
8. Schwarz, T.: An Interpolation Method Maintaining the Wall Distance for Structured and Unstructured Overset Grids. In: Proceedings of the CEAS 2009 European Air and Space Conference, Manchester, UK (2009)
9. Heinrich, R.: Numerical Simulation of Wake-Vortex Encounters Using the Chimera-Technique. In: Wagner, S., Rist, U., Heinemann, H.-J., Hilbig, R. (eds.) New Results in Numerical and Experimental Fluid Mechanics III. NNFM, vol. 77, pp. 74–81. Springer, Heidelberg (2002)
10. Kroll, N., Fassbender, J.K. (eds.): MEGAFLOW — Numerical Flow Simulation for Aircraft Design — Results of the second phase of the German CFD initiative MEGAFLOW, presented during its closing symposium at DLR, Braunschweig, Germany, December 10 and 11, 2002. NNFM, vol. 89. Springer, Heidelberg (2005)

11. De Bruin, A.C.: WAVENC, Wake Vortex Evolution and Wake Vortex Encounter, Publishable Synthesis Report. WAVENC report no. R6 or NLR-TR-2000 (2000)
12. Struijs, R., Jonville, G., Darracq, D., Heinrich, R.: Inviscid Computation of Effect of Wake Vortices on a Scale-Model Airplane. AIAA Journal 40(1), 100–109 (2003)
13. Heinrich, R., Reimer, L., Michler, A., Ritter, M., Neumann, J.: DLR Pilot Applications in ComFliTe. In: Kroll, N., Radespiel, R., van der Burg, J.W., Sorensen, K. (eds.) Computational Flight Testing — Results of the Closing Symposium of the German Research initiative ComFliTe, Braunschweig, Germany, June 11-12. NNFM, Springer, Heidelberg (2012)